ISSN 1674-1056
http://cpb.iphy.ac.cn
http://iopscience.iop.org/cpb
中国物理 B
Chinese Physics
中国物理
Chinese Physics B

Quantitative deformation measurements and analysis of the ferrite-austenite banded structure in a 2205 duplex stainless steel at 250℃

Ji-Hua Liu(刘计划)
Citation: Chin. Phys. B . 2018, 27(3): 038102. **doi:** 10.1088/1674-1056/27/3/038102

Journal homepage: http://cpb.iphy.ac.cn; http://iopscience.iop.org/cpb

What follows is a list of articles you may be interested in

Cyclic stress induced phase transformation insuper-bainitic microstructure

Wencui Xiu(修文翠), Ying Han(韩英), Cheng Liu(刘澄), Hua Wu(吴化), Yunxu Liu(刘云旭)
Chin. Phys. B . 2017, 26(3): 038101. **doi:** 10.1088/1674-1056/26/3/038101

Amorphous phase formation rules in high-entropy alloys

Qiu-Wei Xing(邢秋玮), Yong Zhang(张勇)
Chin. Phys. B . 2017, 26(1): 018104. **doi:** 10.1088/1674-1056/26/1/018104

Detection and formation mechanism of micro-defects in ultrafine pitch Cu–Cu direct bonding

Zi-Yu Liu(刘子玉), Jian Cai(蔡坚), Qian Wang(王谦), Yu Chen(陈瑜)
Chin. Phys. B . 2016, 25(1): 018103. **doi:** 10.1088/1674-1056/25/1/018103

Influence of vacuum degree on growth of Bi_2Te_3 single crystal

Tang Yan-Kun, Zhao Wen-Juan, Zhu Hua-Qiang, Huang Yong-Chao, Cao Wei-Wei, Yang Qian, Yao Xiao-Yan, Zhai Ya, Dong Shuai
Chin. Phys. B . 2015, 24(7): 078101. **doi:** 10.1088/1674-1056/24/7/078101

Settling velocity of equiaxed dendrites in a tube

Zhou Peng, Wang Meng, Lin Xin, Huang Wei-Dong
Chin. Phys. B . 2013, 22(1): 018101. **doi:** 10.1088/1674-1056/22/1/018101

Quantitative deformation measurements and analysis of the ferrite-austenite banded structure in a 2205 duplex stainless steel at 250 °C*

Ji-Hua Liu(刘计划)[1,2,†]

[1] School of Mechanical Engineering, Tianjin University, Tianjin 300354, China
[2] Tianjin Key Laboratory of Modern Engineering Mechanics, Tianjin University, Tianjin 300354, China

(Received 5 September 2017; revised manuscript received 23 December 2017; published online 11 February 2018)

The deformation process of the microstructure in 2205 duplex stainless steel (DSS) under thermo-mechanical coupling at 250 °C was investigated using digital image correlation (DIC). A thermal tension test of duplex stainless steel (2205DSS) with a banded structure was carried out to observe the initial deformation of the microstructure. It was found that inhomogeneous strain fields occurred primarily in austenite. The maximum normal strain in austenite was almost positive, while that in ferrite was almost negative. In addition, a thermal cyclic-loading test was conducted, and the strain field was characterized by e_{11}. Strain heterogeneities were induced after 400 cycles, which spread within the austenite and at the phase boundaries with the load increasing. The high tensile-strain regions were always located adjacent to regions of intense compressive strain. Based on the strain matrix sum vs. cycle number, we found that hardening occurred in the early cycles followed by softening.

Keywords: thermo-mechanical coupling, duplex stainless steel, digital image correlation (DIC)

PACS: 81.70.–q, 81.70.Fy, 81.05.Bx, 81.40.Lm **DOI:** 10.1088/1674-1056/27/3/038102

1. Introduction

Duplex stainless steel (DSS), which consists of about the same amount of ferrite and austenite, combines the characteristics of ferritic and austenitic stainless steels. Because of its high strength, good corrosion resistance, and other improved mechanical properties, DSS has become a good alternative to the single-phase (austenitic or ferritic) steel[1–3] in many industrial applications, such as nuclear power plants, chemical industry, pipes for heat exchangers, offshore applications, and other general engineering applications.[4–6]

Body-centered-cubic (bcc) ferrite and face-centered-cubic (fcc) austenite have different mechanical properties, which results in different deformation behaviors of DSS on the micro scale. The deformation properties of the two phases affect not only each other but also the load transfer characteristics, which can cause strain and stress partitioning.[7] Because of the different thermal expansion coefficients of ferrite and austenite, the residual micro-stress is always present in DSS. Micro-stress in duplex microstructures changes during deformation because of the different elasto-plastic properties of the two phases, which likely affects both plastic strain and strain localization.[8] In recent years, the micro-behavior of duplex stainless steel has been studied widely and intensely.[9–17] Duplex stainless steel is generally used below 316 °C according to the ASME boiler and pressure vessel code[18] because of the risk of precipitation of embrittling phases. However, the embrittlement phenomenon of DSS can already occur at 250 °C.[19] Quantitative micro-deformation measurements and analysis of 2205DSS at about 250 °C are required for many applications. Few studies focus on the micro-deformation behavior of 2205DSS in this temperature range.

In this paper, we investigated both the initial micro-deformation characteristics and the cyclic loading response of 2205DSS under thermo-mechanical coupling at 250 °C. The microstructure of the surface was observed in real-time during quasi *in-situ* loading using a scanning electron microscope (SEM). Furthermore, the surface micro-deformation was calculated via digital image correlation (DIC),[19–23] which used real-time images taken during thermal tension and thermal cyclic-loading tests. The micro-deformation mechanism in this temperature range can be better understood through surface observation and surface deformation measurements. The observation and analysis of the micro-deformation enables the optimization of both the material performance and the microstructure for the application of DSS in challenging environments.

2. Materials and methods

2.1. The basic principle of digital image correlation

In DIC, the displacement/strain information is obtained by comparing the deformed image with the reference image

*Project supported by the National Natural Science Foundation of China (Grant Nos. 11472187 and 11602166), the National Basic Research Program of China (Grant No. 2014CB046805), and the Natural Science Foundation of Tianjin, China (Grant No. 16JCYBJC40500).

†Corresponding author. E-mail: jhliu08lx@126.com

© 2018 Chinese Physical Society and IOP Publishing Ltd

using a correlation algorithm.[24] Artificial speckles/textures of samples can be used to provide the deformation information. These can be obtained by tracking/matching the same pixel points between reference and deformed images. As shown in Fig. 1, before computing the displacement of a point P, a square reference subset with center P in the reference image is chosen. Subsequently, tracking the corresponding location (P') of P in the deformed image is performed. In order to determine the degree of matching between the reference and the deformed subset, a corresponding correlation-criterion is predefined. By searching for the position with the maximum correlation coefficient, the deformed subset can be determined and the displacement of P is obtained.

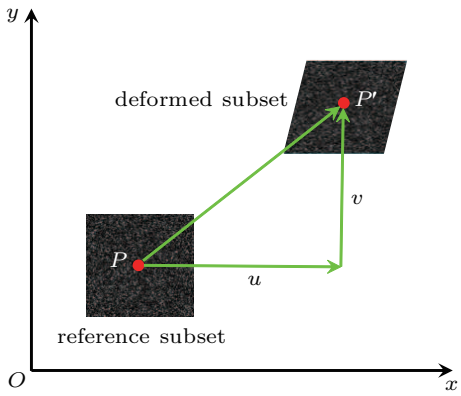


Fig. 1. (color online) Schematic illustration of the basic principle of DIC.

2.2. Materials and samples

Steel 2205DSS with a banded microstructure was provided by Zewee industrial co., LTD (Shanghai, China). The chemical composition is shown in Table 1. Both shape and size of the samples are shown in Fig. 2(a). The samples were polished with 3000-grit SiC paper followed by a 2.5 μm polishing finish with diamond paste. In order to expose the microstructure, the samples were etched in a solution of HCl, HNO_3, and H_2O with a volume ratio of 3:1:20.

Table 1. Chemical composition (wt.%) of the investigated 2205 duplex stainless steel.

C	Si	Mn	P	S	Cr	Ni	Mo	N
0.025	0.6	1.5	0.026	0.001	22.5	5.8	3.0	0.16

2.3. Thermal tests

A GATAN MTEST 5000W *in-situ* micro-tension stage with a heating function and cooling system attached to a ZEISS EVO MA15 scanning electron microscope was used for loading and orientation imaging microscopy, as shown in Fig. 2(b). The SEM images were fed into a DIC system (Vic-2D 2009, Correlated Solutions, Columbia, SC, USA) to calculate the displacement and strain. A secondary electron detector was used for the SEM study, with a voltage of 20 kV and a working distance of 16 mm.

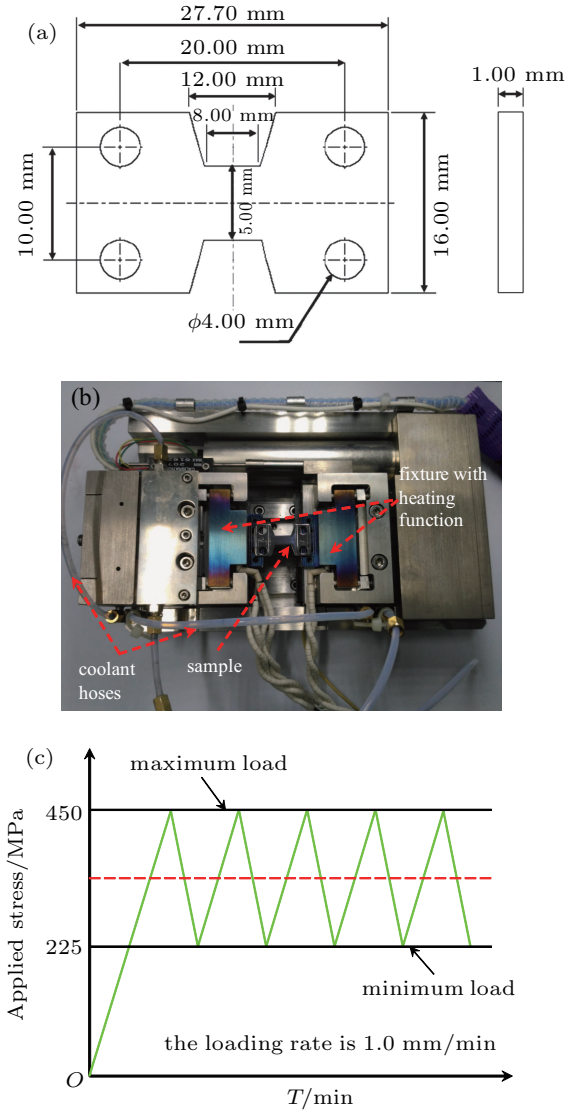


Fig. 2. (color online) (a) Shape and size of the samples; (b) GATAN MTEST 5000W *in-situ* micro-tension stage with a heating function and cooling system; (c) schematic illustration of the loading route for the cyclic-loading test.

Mechanical testing was conducted when the sample was heated to and kept at 250 °C. The tests were carried out at a speed of 1.0 mm/min, and SEM images were captured in succession. One of the images was used as the reference image, while the other images were treated as the deformed images. Pristine texture images of the sample surface were used for the correlation calculation of DIC.

A series of zero-deformation tests were performed to observe and analyze the system errors. The system errors primarily resulting from drift and any spatial distortion in the SEM images should be determined first.[25,26] Hence, the zero-deformation tests were performed. Nine images were captured in succession and with different magnifications at 250 °C. The first image was used as the reference image. Subsequently, the mean and standard deviation of the displacements were determined.

Next, a 2205DSS sample with the banded structure was used to study the initial deformation response of the microstructure. The (ferrite and austenite) deformation of the microstructure in this experiment was characterized using maximum normal strain, which is denoted by $e_{\max.n}$. An image captured at 300 MPa, instead of 0 MPa, was then taken as the reference image. This was done because the sample surface shifted relative to the image acquisition window of the SEM with the load increasing during the experiments. The shifts were probably due to sample clamping, magnification of images, and sample deformation. Macro-strain was small at 300 MPa due to the high Young modulus (about 190 GPa) of the 2205DSS. Thus, selecting the image captured at 300 MPa as the reference was non-critical.

Subsequently, a cyclic-loading test was performed to study the cycling response of the microstructure of 2205DSS with banded features. The strain fields were characterized by e_{11}. The deformed images were captured at 400, 1000, 4000, 5000, 9000, 13000, and 14000 cycles, respectively. The image captured before the cyclic loading test at 250 °C was used as the reference image. The loading route for the cyclic-loading test is shown in Fig. 2(c).

The main parameters for DIC are described below. The calculation step was 5 pixels, and the size of the subset was 61×61 pixels, which were kept unchanged during all experiments. The size of the region of interest (ROI) was 451×401 pixels during the thermal tension test but 851×556 pixels during the thermal cyclic-loading test. Furthermore, the stress-controlled cyclic loading test ($R = 0.5$) with nonzero mean-stress was performed using a GATAN MTEST 5000W *in-situ* micro-tension stage with a maximum load of 450 MPa.

3. Results and discussion

3.1. Zero-deformation tests

The mean and standard deviation of the displacements are shown in Fig. 3. The results demonstrate the accuracy and robustness of DIC.[21] Figures 3(a) and 3(b) are the mean displacements with standard deviations for the u and v fields. Figures 3(c) and 3(d) are the standard deviations for the u and v fields. The mean displacements and standard deviations increased with time. However, the maximum absolute value was less than 0.06 pixel, which was used as the system error. This was sufficient to meet the accuracy and robustness requirement for this study.

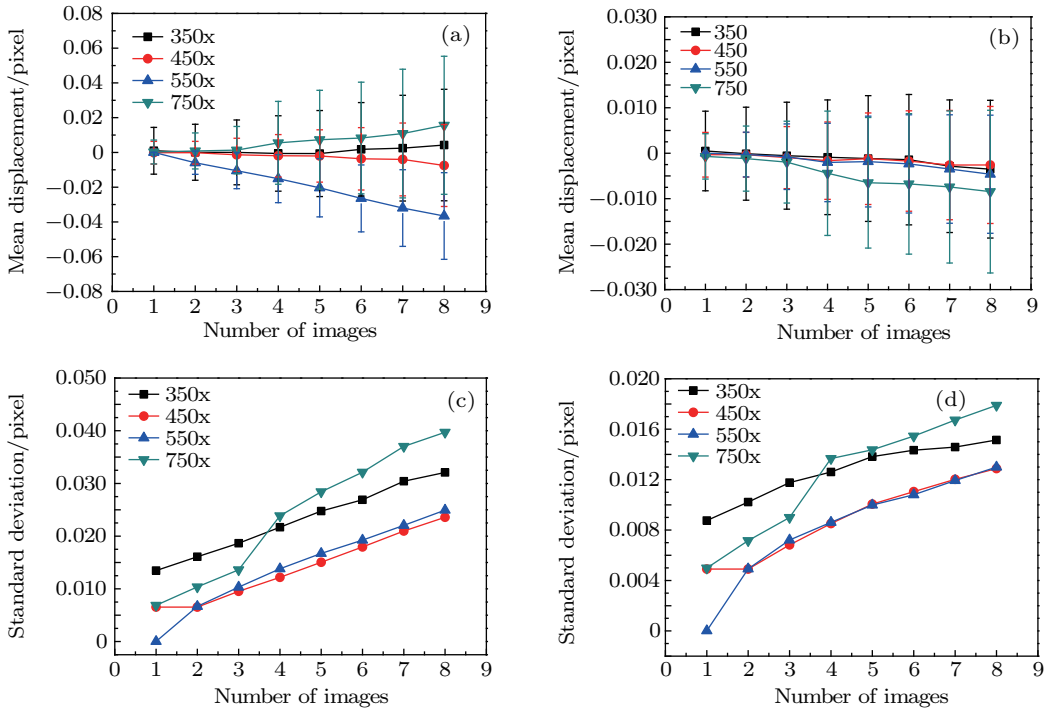


Fig. 3. (color online) Mean displacements with standard deviations for (a) the u field and (b) the v field. Standard deviations for (c) the u field and (d) the v field.

3.2. Thermal tension tests

The maximum normal strain maps of the microstructure obtained using DIC are shown in Fig. 4. Both ROI and loading direction can be seen in Fig. 4(a). Figures 4(b)–4(e) are the strain maps at different applied stresses σ_p (360 MPa, 380 MPa, 440 MPa, and 480 MPa). The white lines in Fig. 4 mark the interfaces between the two phases. As shown in Fig. 4, after a small load of 360 MPa was applied, inhomogeneous strain fields primarily appeared in the austenite phases. When the stress reached 380 MPa, 440 MPa, and 480 MPa, most strain heterogeneities were still within the austenite regions. The inhomogeneous strain fields, however, became

more intense. Furthermore, figure 4 reveals that, in the ferrite regions, the strain distribution was more homogeneous than that in the austenite regions. In addition, unlike the phenomenon found in the tension tests at room temperature,[7] the maximum normal strain in austenite was almost positive, while it was almost negative for ferrite, as shown in Fig. 4. In other words, the strain fields in austenite were larger than those in ferrite.

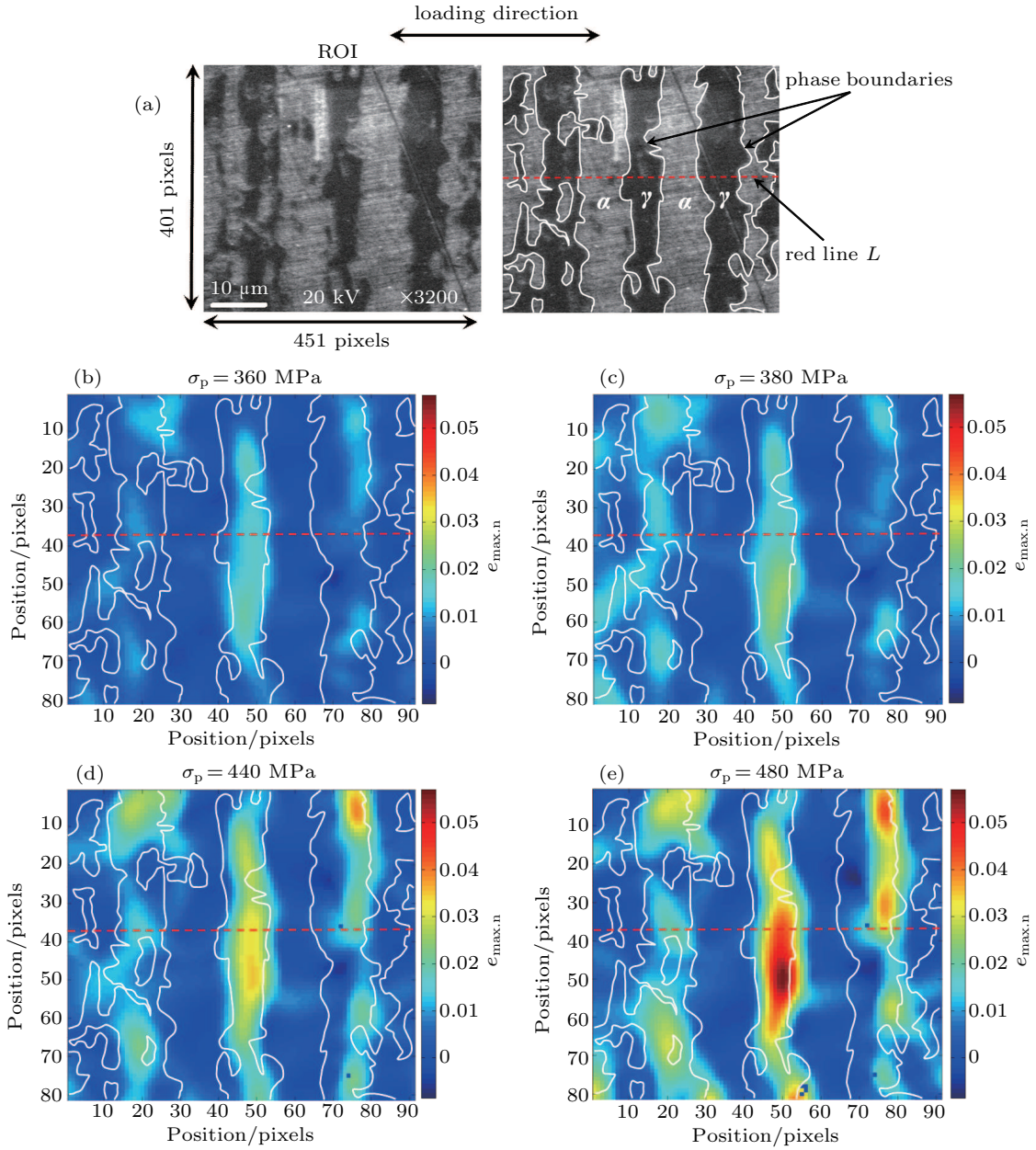


Fig. 4. (color online) (a) ROI in this experiment, the light phase is ferrite (α-phase) and the dark phase is austenite (γ-phase). Maximum normal strain at (b) 360 MPa, (c) 380 MPa, (d) 440 MPa, and (e) 480 MPa.

The data along the red line L shown in Fig. 4 are plotted in Fig. 5(a) to provide a better visualization of the strain distribution. According to the approximate locations of the phase boundaries, the curves in Fig. 5 are divided into several parts, which are related to ferrite and austenite (α- and γ-phase). Strains in the periphery of the ROI are not taken into account in the discussion because of the boundary effects. Thus, the locations of α_1 and γ_5 are neglected in the following analysis. Throughout the measurement range, the maximum strain occurred primarily in austenite close to the phase boundaries. The minimum values were found in ferrite. Figure 5 further illustrates the analyses of the strain distribution of the 2205DSS with a banded structure in the thermal tension above. Two phases were subjected to the same macro-stress in the loading direction because the austenite islands were embedded in the ferrite matrix and the directions of the banded structures were perpendicular to the loading direction. In addition, because the elastic modulus of ferrite is larger than that of austenite, the austenite phases undergo more deformation than ferrite. Figure 5(b) shows the development of the strain

matrix sum with increasing applied stress, which can be obtained by calculating the sums of the maximum normal strain matrices of the microstructure at different stress states, which are denoted by $S_{\max.n}$.

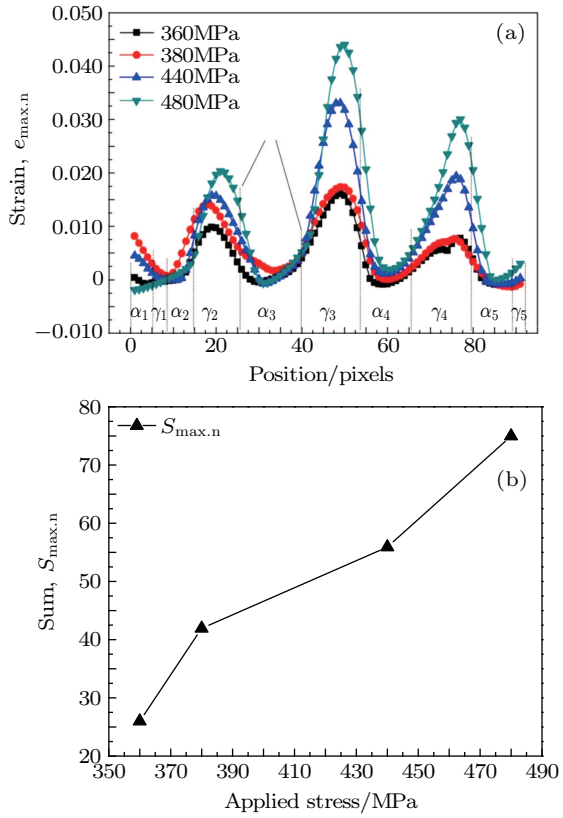


Fig. 5. (color online) (a) Strain curves based on the data extracted from the red line L in the strain contour at different stress states; (b) sum of strain matrix vs applied stress.

As shown in Fig. 4, more and larger strain heterogeneities were present in austenite than those in ferrite. One reason for this is that ferrite is stiffer than austenite. Another reason is that the two phases in duplex stainless steel have different thermal expansion coefficients,[27] which produces tensile micro-stress in austenite and compressive micro-stress in ferrite under these thermal conditions. Thus, the tensile micro-stress increases the tensile deformation in austenite, while the compressive micro-stress suppresses the tensile deformation in ferrite. Due to the greater stiffness of ferrite, during the thermal tension tests, the compressive strain occurred in ferrite during the initial deformation stage. Therefore, it is expected that more strain appears in austenite.

Overall, during the thermal tension tests, the deformation of ferrite was delayed and the deformation of austenite accelerated. This was due to different micro-stresses generated by the different thermal expansion coefficients between the two phases. This caused a sharp contrast in the strain fields between the two phases, which generated high strain gradients, as shown in Fig. 4. Since the deformation of ferrite was partly suppressed in the thermal tension tests, the strain in ferrite would be small in the initial deformation stage. Compared to the relative large strain in austenite, the strain fields in ferrite were more homogeneous.

Figure 6 shows the true stress–strain curves during the tension tests at room temperature and 250 °C. The tensile property at 250 °C decreased significantly. In particular, the curve at 250 °C had no clear yield stage compared to room temperature. The yield strength, ultimate strength, and plasticity at 250 °C were much smaller than those at room temperature. This means that plastic deformation can take place earlier and material failure occurs more rapidly in 2205DSS at 250 °C.

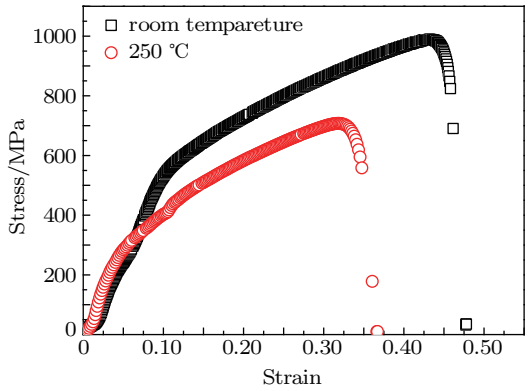


Fig. 6. (color online) The true stress–strain curves of as-received 2205DDS according to the tension tests at room temperature and 250 °C.

3.3. Thermal cyclic-loading tests

Figure 7 shows the strain distribution development of the microstructure for different cycles. In the specific case of strain fields, strain heterogeneities have been induced after 400 cycles. Subsequently, the heterogeneities for the following cycles spread and became more apparent. They mainly accumulated in austenite and at the phase boundaries. The strain fields in ferrite, however, were relatively homogeneous. It is worth mentioning that an intense tensile strain region was always observed adjacent to an intense compressive strain region of similar magnitude. Moreover, the apparent contrast and small spacing led to high strain gradients. Specifically, in zones 1–3 marked in Fig. 7(a), the area and size of strain localization increased with the number of cycles. Then, it remained practically unchanged after 9000 cycles with only slight fluctuations in magnitude.

It is well known that micro-stresses must balance between phases, while residual stresses are self-balanced.[27] The strain field obtained by DIC is a type of accumulated residual micro-deformation. In other words, the strain fields are also balanced. To validate the strain fields obtained by DIC, the mean values (M_{11}) of the strain matrices were calculated, as shown in Fig. 8(a). The absolute numbers for the mean values were below 0.1%.

These phenomena in the thermal cyclic-loading test are related to the difference between the elasto-plastic properties and thermal expansion coefficients. However, they are also related to the crystallographic orientation relationships and slip system difference between neighboring ferrite and austenite. The reason that the area and size of strain localization in zones 1–3 increased with the number of cycles (see Fig. 7) is that micro-strain accumulated gradually in certain areas. These areas are generally grain or phase boundaries. More specifically, if the Kurdjumov–Sachs relationship is not satisfied, the strain will be arrested at the corresponding grain or phase boundaries. After many cycles, the arrested strain cannot spread through neighboring grains because of the different slip systems that cause strain accumulation. Therefore, strain localization becomes increasingly intense with increasing cycle numbers in these areas. The strain localization can indicate the stress localization under certain circumstances. In other words, the high strain localization correlates potential microcrack nucleation sites.

The sums of the strain matrices were studied, as shown in Fig. 8(b). These can be obtained by calculating the sums of the von Mises equivalent strain matrices after different cycles, which are denoted by $S_{\text{Mises.e}}$. The sum vs. number of cycles shows that hardening occurred before 4000 cycles, followed by softening. The first hardening stage generally occurs due to work-hardening in austenite. This, in turn, is due to planar slip from nitrogen alloying and the lower stiffness. Nitrogen, which has low solubility in ferrite and is mainly present in austenite, can cause the duplex stainless steel to show apparent hardening. Nitrogen can change the slip mode of austenite from wavy to planar, which is one of the reasons for the 12 closely-packed slip-systems in austenite. The slip systems can increase the dislocation mobility in austenite in almost all crystallographic directions.

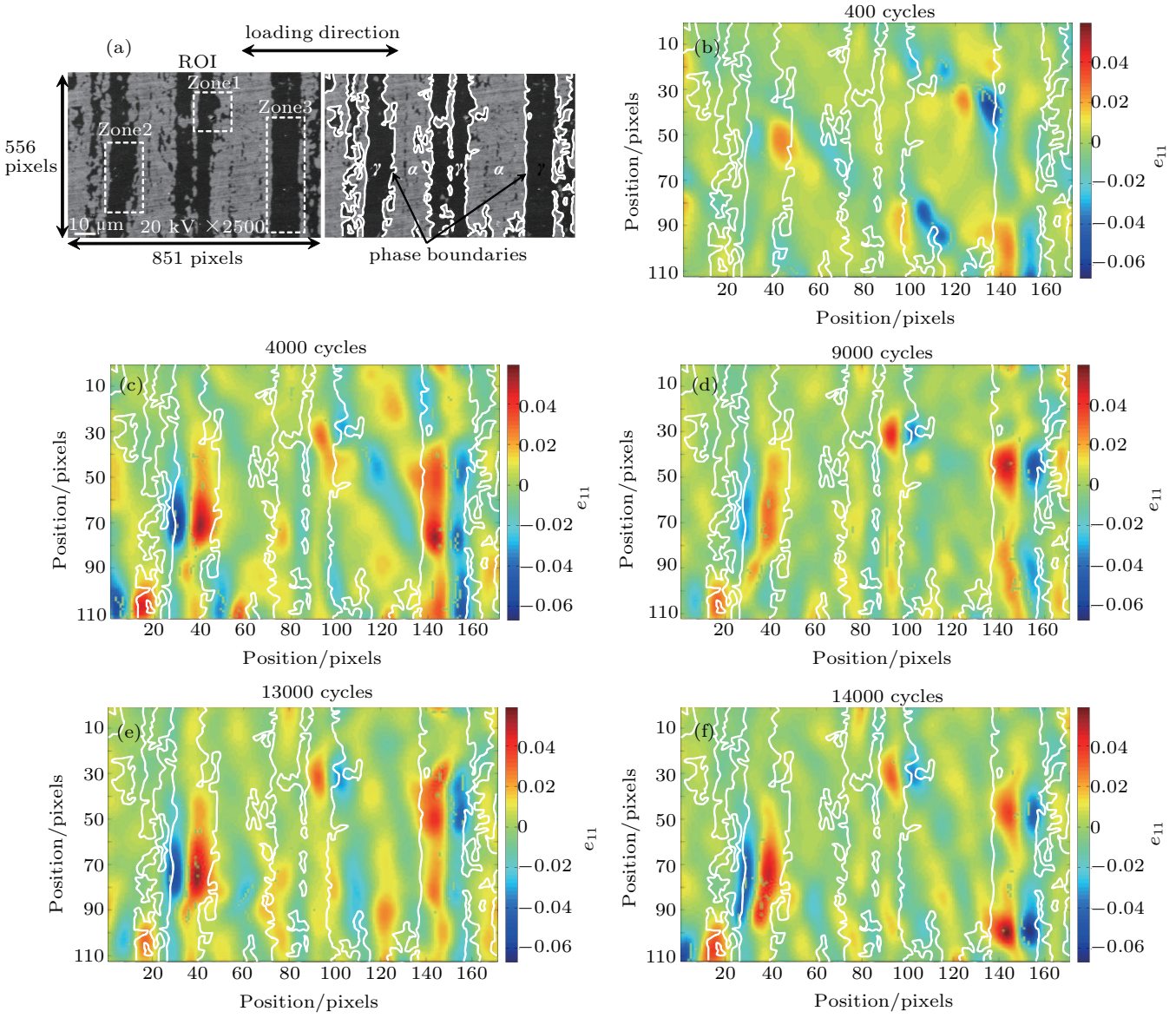


Fig. 7. (color online) (a) ROI in the reference image, the light phase is ferrite (α-phase) and the dark phase is austenite (γ-phase). Strain distributions after (b) 400 cycles, (c) 4000 cycles, (d) 9000 cycles, (e) 13000 cycles, and (f) 14000 cycles.

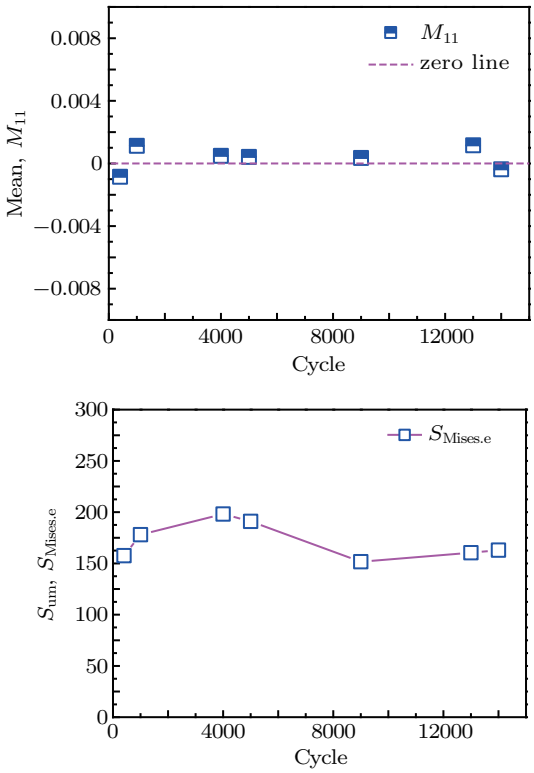


Fig. 8. (color online) (a) Mean of the strain matrices for different cycles. (b) Sum of the strain matrices after different cycles.

4. Conclusion

The behavior of 2205 duplex stainless steel under thermo-mechanical coupling was studied using digital image correlation. The results can be summarized as follows.

To observe the initial deformation response of the microstructure of 2205DSS under thermo-mechanical coupling, as-received 2205DSS with a banded structure was studied in a thermal tension test. The inhomogeneous strain fields occurred predominantly in austenite and occasionally at the phase boundaries. This is similar to the results observed in the tension test at room temperature. However, the decisive difference is that the maximum normal strain was almost positive in austenite and negative in ferrite, which is mainly due to the different thermal expansion coefficients. After comparing the true stress–strain curve at 250 °C with that at room temperature, we found that the plasticity, yield, and ultimate strength significantly decreased at 250 °C.

The development of strain distribution of the microstructure in as-received 2205DSS with a banded structure was studied during the thermal cyclic-loading test. It was found that both magnitude and size of the strain localization increased with increasing cycle numbers in austenite and at the phase boundaries. This is attributed to micro-strain accumulation due to strain arrested at the grain or phase boundaries. For these boundaries, the Kurdjumov–Sachs relationship was not satisfied. Furthermore, an intense tensile strain region was always found to be adjacent to an intense compressive strain region of similar magnitude. In addition, hardening occurred within 4000 cycles followed by softening. The hardening stage is due to work-hardening in austenite.

In summary, it was shown that DIC in combination with SEM can be used to analyze the micro-deformation of 2205DSS at 250 °C. The results with respect to the micro-deformation behavior of 2205DSS under thermo-mechanical coupling improve the understanding of many properties of DSS.

References

[1] Sun G X, Jiang Y, Zhang X R, Sun S C, Jiang Z H, Wang W Q and Lian J S 2017 *Chin. Phys. B* **26** 096104
[2] Sun S C, Sun G X, Jiang Z H, Ji C T, Liu J A and Lian J S 2014 *Chin. Phys. B* **23** 026104
[3] Li C X, Dang S H, Wang L P, Zhang C L and Han P D 2014 *Chin. Phys. B* **23** 037102
[4] Gunn R N 2003 *Duplex Stainless Steel-Microstructure, Properties, and Applications* (2nd Edn.) (Cambridge: Abington Publishing) pp. 175–184
[5] Filho A I, Rollo J M D A, Silva R V and Martinez G 2005 *Mater. Lett.* **59** 1192
[6] Gurrappa I and Malakondaiah G 2006 *Metall. Mater. Trans. A* **37** 3039
[7] Örnek C and Engelberg D L 2016 *J. Strain Anal. Eng.* **51** 207
[8] Johansson J, Odén M and Zeng X H 1999 *Acta Mater.* **47** 2669
[9] Zhang B B, Jiang Z H, Li H B, Zhang S C, Feng H and Li H 2017 *Mater. Charact.* **129** 31
[10] Farnoush H, Momeni A, Dehghani K, Mohandesi J A and Keshmiri H 2010 *Mater. Design* **31** 220
[11] Michalska J and Sozańska M 2006 *Mater. Charact.* **56** 355
[12] Wu H C, Yang B, Shi Y Z, Gao Q and Wang Y Q 2015 *J. Mater. Sci. Technol.* **31** 1144
[13] Yang Y and Yan B 2013 *Mater. Sci. Eng. A* **579** 194
[14] Chiu P K, Weng K L, Wang S H, Yang J R, Huang Y S and Fang J 2005 *Mater. Sci. Eng. A* **398** 349
[15] Stevens K J 2013 *Mater. SCI. Tech-lond.* **15** 903
[16] Silva R, Baroni L F S, Silva M B R, Afonso C R M, Kuri S E and Rovere C A D 2016 *Mater. Charact.* **114** 211
[17] Young M C, Tsay L W, Shin C S and Chan S L I 2007 *Int. J. Fatigue.* **29** 2155
[18] Boiler A and Code P V 1998 *ASME Boiler and Pressure Vessel Code* (New York: American Society of Mechanical Engineers) p. 1432
[19] Bartali A E, Aubin V and Degallaix S 2008 *Fatigue Fract. Eng. M.* **31** 137
[20] Zhang X C, Yang G, Zhan N and Ji H W 2015 *Appl. Opt.* **54** 934
[21] Zhang X C, Wang Y, Yang J, Qiao Z X, Ren C H and Chen C 2016 *Opt. Laser. Eng.* **85** 24
[22] Bartali A E, Aubin V and Degallaix S 2009 *Int. J. Fatigue* **31** 2049
[23] Ren C H, Zhang X C, Ji H W, Zhan N and Qiao Z X 2017 *Mat. Sci. Eng. A* **705** 394
[24] Pan B, Qian K M, Xie H M and Asundi A 2009 *Meas. Sci. Technol.* **20** 152
[25] Sutton M A, Li N, Joy D C, Reynolds A P and Li X 2007 *Exp. Mech.* **47** 775
[26] Sutton M A, Li N, Garcia D, Cornille N, Orteu J J, McNeill S R, Schreier H W, Li X and Reynolds A P 2007 *Exp. Mech.* **47** 789
[27] Johansson J and Odén M 2000 *Metall. Mater. Trans. A* **31** 1557